Liquid Crystals
Publication details, including instructions for authors and subscription information:
http://www.informaworld.com/smpp/title~content=t713926090

Effect of terminal functional group size on ferroelectric and antiferroelectric properties of liquid crystals

Stephen J. Cowling[a]; Alan W. Hall[a]; John W. Goodby[a]
[a] Department of Chemistry, The University of York, Heslington, York YO10 5DD, UK

To cite this Article Cowling, Stephen J. , Hall, Alan W. and Goodby, John W.(2005) 'Effect of terminal functional group size on ferroelectric and antiferroelectric properties of liquid crystals', Liquid Crystals, 32: 11, 1483 — 1498
To link to this Article: DOI: 10.1080/02678290500252360
URL: http://dx.doi.org/10.1080/02678290500252360

Liquid Crystals, Vol. 32, No. 11–12, November–December 2005, 1483–1498

Effect of terminal functional group size on ferroelectric and antiferroelectric properties of liquid crystals

STEPHEN J. COWLING, ALAN W. HALL and JOHN W. GOODBY*
Department of Chemistry, The University of York, Heslington, York YO10 5DD, UK

(*Received 1 June 2005; accepted 23 June 2005*)

Through the incorporation of sterically hindering, bulky terminal groups into the structures of chiral and racemic smectic liquid-crystalline materials, we sought to interfere with, and decouple, the layers of various mesophases. By varying the size of the terminal group we found that we could control the mesophase structure, and to some degree its physical properties. In this article we present textural and X-ray data which give insights into the structures of the mesophases.

1. Introduction

The basic molecular design of ferroelectric and antiferroelectric liquid crystals usually involves the incorporation of a central aromatic or heterocyclic core unit, which is sandwiched between two terminal aliphatic chains [1]. When molecules with this type of architecture self-organize they do so with their rigid, aromatic parts packing together and the flexible/dynamic aliphatic chains likewise orienting together; thereby the overall system becomes effectively microphase-segregated into layers.

In the development of ferroelectric and antiferroelectric liquid crystals for microdisplays, based on liquid crystal over silicon technologies (LCOS), the main target of material design has been, by default, the variation in the structure of the central core, in the belief that the core is more important in influencing mesophase incidence, mesophase temperature range, isotropization point, melting point, mesophase sequence, tilt angle, magnitude of the spontaneous polarization, and the reorientational viscosity associated with the mesophase. However, few systematic studies have been reported where the terminal positions of the aliphatic chains have been substituted with bulky or polar groups. Over ten years ago we began our initial investigations of this type of molecular design, and our studies clearly demonstrate that the nature of the terminal group and the intermolecular interactions which occur at the layer interfaces are critically important in determining the physical properties of a material [2]. Here we report on the effects of a systematic increase in the steric bulk of an apolar terminal unit on mesophase stability and material properties.

Figure 1 shows a molecular template, based on the classical biphenyl-phenyl esters system [3, 4], for the design of ferroelectric and antiferroelectric liquid crystals reported in this study. Apart from varying the size of the terminal group, we maintained the rest of the molecular structure of the materials prepared so that we could make direct comparisons of the physical properties and structures of the mesophases. The terminal group was varied from an allyl unit to a cyclopropyl moiety through to a cycloheptyl ring, and then to the more rigid norbornyl and adamantyl moieties. In order to demonstrate the steric bulks of these moieties relative to one another and to the phenyl rings of the aromatic unit, space filling models of the terminal groups are shown together for comparison in figure 2. In the following sections we report on the syntheses, the structures and phase transitions of the mesophases, and the physical properties of these materials.

In addition to investigating the effect of terminal group size on mesomorphic properties, this study also provides an opportunity to explore the structure at the interface between the layers in smectic phases, particularly in relation to the induced curvature introduced by the packing together of the bulky terminal groups. Such packing arrangements might induce long range modulated structures, examples of which include the smectic A and smectic C antiphases ($\tilde{A}$ and $\tilde{C}$) [5]; two-dimensional modulated phases, as found for the undulating twist grain boundary ($UTGB_C$), phase [6]; and disordered cluster structures exhibited as rafts in biological membranes [7].

*Corresponding author. Email: jwg500@york.ac.uk

Liquid Crystals
ISSN 0267-8292 print/ISSN 1366-5855 online © 2005 Taylor & Francis
http://www.tandf.co.uk/journals
DOI: 10.1080/02678290500252360

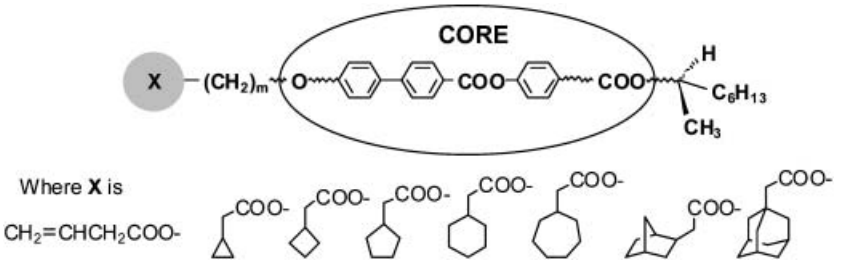

Figure 1. Template design for conventional ferroelectric and antiferroelectric liquid crystals.

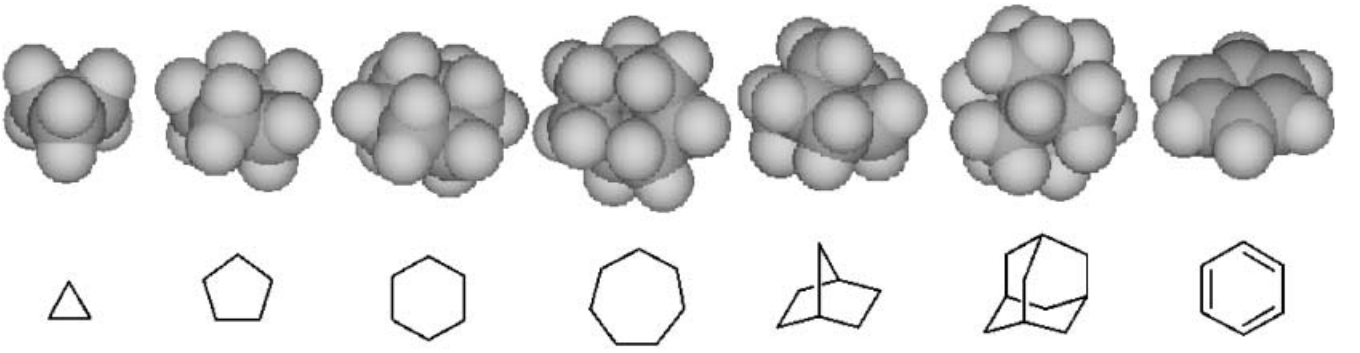

Figure 2. The steric shapes and sizes of the terminal groups in comparison with a phenyl ring.

The diagnosis cartoons in figure 3 show a comparison between how a normal smectic layer might appear, figure 3 (*a*), and how the inter-layer organization might appear with the incorporation of bulky or chemically dissimilar groups, shown as discs, at the terminal positions of the structures in the molecules. In figure 3 (*b*) we have pictured the structure of the mesophase with as many molecules pointing up as there are down and homogeneously distributed within the layer. Structural variations could exist at one extreme with clusters of up and down molecular species forming an inhomogeneously ordered system (rafts), figure 3 (*c*), through to fully 2D modulated structures, figure 3 (*d*). All of these arrangements would, of course, have profound effects on mesophase structure, the arrangements of the molecules in their layers, and the ensuing physical properties.

2. Experimental

In the following section, in order to fully explore the synthetic pathways, we describe the preparation of a

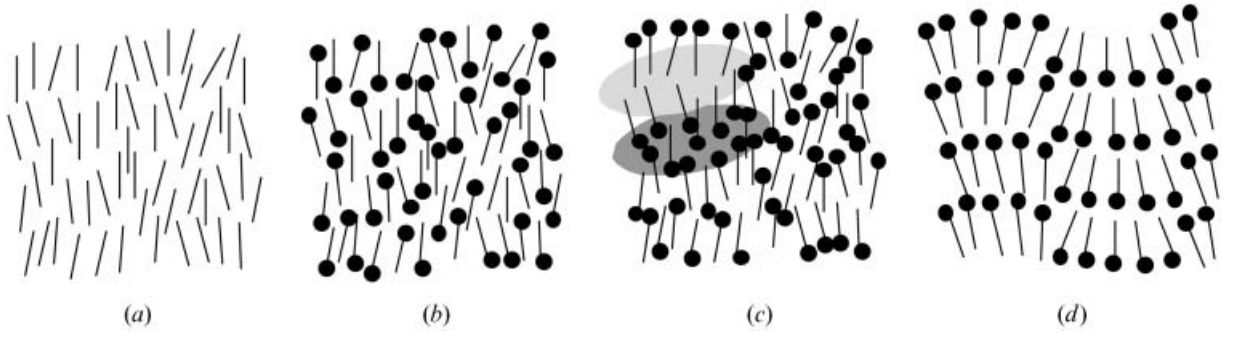

Figure 3. (*a*) The disorganized layer structure of a typical smectic A liquid crystal with the molecules shown as rods; (*b*) the disorganized layered structure of a smectic A where the molecules have bulky end groups; (*c*) clustering of tails and head groups (rafts) to give an inhomogeneous layer structure (highlighted in grey); (*d*) in-plane ordering of the molecules caused by the induced curvature of the packing of the bulky end groups together, the modulation being one-dimensional or two-dimensional within the layer.

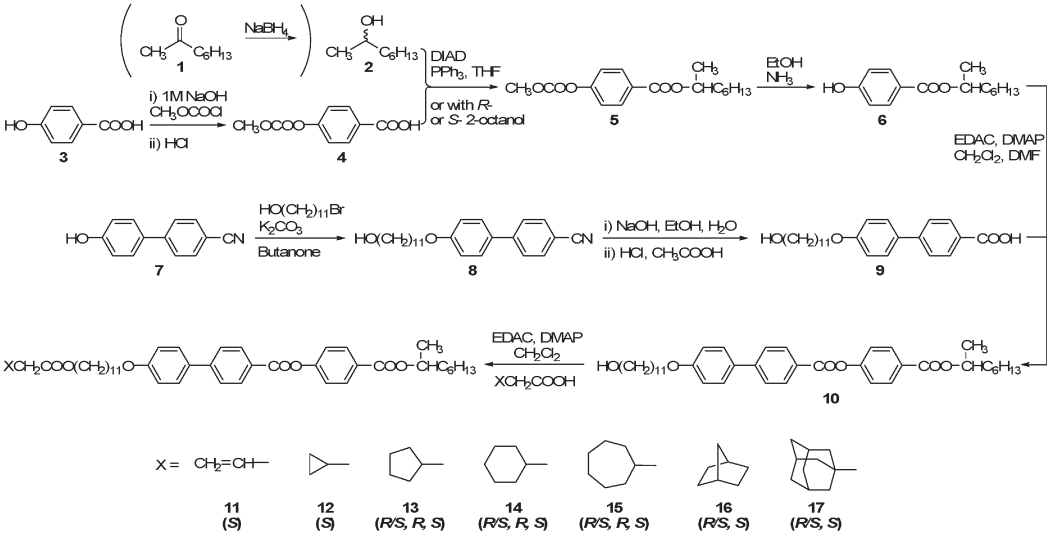

Scheme 1. The synthesis of the racemic materials **13**–**17**(*R*/*S*); similarly the same process can be employed using optically active alcohols to produce the enantiomeric forms of **11** to **17**.

racemic material in detail, starting with the reduction of 2-octanone. The chiral enantiomers were prepared by an identical route except that the *R*- or *S*- 2-octanols were used to replace the racemic modification of 2-octanol derived from the reduction of 2-octanone.

2.1. *Synthesis of materials*

The following synthetic pathway, see scheme 1, for the preparation of racemic modification **14**(*R*/*S*) is representative of all of the target materials shown in table 1. For the racemate **14**(*R*/*S*), the synthesis was achieved using different sources of racemic octan-2-ol, **2** (Aldrich, Avocado), and also through the reduction of 2-octanone, **1**, using $NaBH_4$ as shown in the scheme. Analysis of the octan-2-ol derived from the reduction of 2-octanone by chiral GC showed, within the limits of experimental error, that the enantiomers were formed in equal proportions. For the synthesis of the individual enantiomers the racemic octan-2-ol was replaced by optically active (*R* or *S*) octan-2-ol (Aldrich) at steps 4 to 5 in the scheme.

Phenol **6** was prepared by standard methods starting from 4-hydroxybenzoic acid, **3**. The hydroxy group was first protected as the carbonate to give **4**, this intermediate was esterified with octan-2-ol, **2**, in the presence of diisopropyl azodicarboxylate (DIAD), triphenylphosphine and THF to give **5**. Ester **5** was deprotected using a mixture of ammonia and ethanol to generate the phenol **6** [8]. Analysis by chiral GC of the phenols derived from both the commercial and freshly prepared racemic octan-2-ol, **2**, revealed an equal

Table 1. Elemental analyses, mass ions and enantiomeric excesses for the final products.

Compd Number	%C (found)	%H (found)	%C expected	%H expected	MS (*m*/*z*)	ee
11 (*S*)	75.32	8.46	75.41	8.24	684 (M^+)	0.88
12 (*S*)	75.44	8.64	75.61	8.36	698 (M^+)	0.88
13 (*R*/*S*)	75.79	8.89	76.00	8.60	860 (M^+)	0.00
13 (*R*)	75.84	9.03	76.00	8.60	727 (M^+)	0.92
13 (*S*)	76.30	8.86	76.00	8.60	726 (M^+)	0.88
14 (*R*/*S*)	76.11	8.92	76.18	8.71	741 (M^+)	0.00
14 (*R*)	76.22	8.70	76.18	8.71	741 (M^+)	0.92
14 (*S*)	76.40	8.92	76.18	8.71	741 (M^+)	0.88
15 (*R*/*S*)	76.62	9.05	76.36	8.81	754 (M^+)	0.00
15 (*R*)	76.62	9.10	76.36	8.81	755 (M^+)	0.92
15 (*S*)	76.61	9.17	76.36	8.81	754 (M^+)	0.88
16 (*R*/*S*)	76.70	8.81	76.56	8.57	752 (M^+)	0.00
16 (*S*)	76.44	8.87	76.56	8.57	752 (M^+)	0.88
17 (*R*/*S*)	77.66	8.66	77.24	8.64	792 (M^+)	0.00
17 (*S*)	77.43	8.94	77.24	8.64	792 (M^+)	0.88

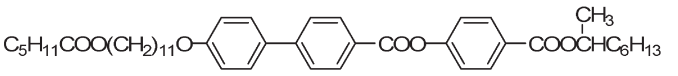

18

distribution of enantiomers within the limits of the experiment (i.e. $ee = 0.0 \pm 0.5\%$). In addition, the optical rotations of the racemic materials prepared were all found to be zero.

Compound **9**, 4′-(11-hydroxyundecyloxy)biphenyl-4-carboxylic acid, was prepared starting from 4-cyano-4′-hydroxybiphenyl, **7**, which was first alkylated with 11-bromoundecan-1-ol in the presence of potassium carbonate in butanone, followed by base hydrolysis of the nitrile.

Compounds **6** and **9** were esterified in the presence of 1-(3-dimethylaminopropyl)-3-ethyl carbodiimide.HCl (EDAC) and 4-(dimethylamino)pyridine (DMAP) to give **10**. Under these conditions **10** is formed with no self-esterification. The last step in the pathway was the esterification, under the same conditions, of **10** with one of the selected acids (XCH_2COOH) to give products **11** to **17**.

In addition to the target materials, the following compound was prepared so that direct comparisons could be made with materials not possessing bulky end groups as in the case of **18**. Compound **18** was prepared using the same procedure except that compound **10** was esterified with hexanoic acid. Compound **18** is listed in table 4, along with structurally related materials.

2.1.1. 4-Cyano-4′-(11-hydroxyundecyloxy)biphenyl, 8. 4-Cyano-4′-hydroxybiphenyl (8.22 g, 0.042 mol) **7**, 11-bromo-1-undecanol (10.0 g, 0.040 mol) and potassium carbonate (23.0 g, 0.170 mol) were heated under reflux in dry butanone (125 ml) for 15 h. The solids were removed by filtration and washed with acetone (2×50 ml). The combined solvents were removed *in vacuo* to give a white solid which was recrystallized from acetonitrile. Yield 14.31 g (93%). ^{1}H NMR ($CDCl_3$): δ 1.30 (12H, m), 1.50 (5H, m), 1.80 (2H, quint), 3.64 (2H, t), 4.00 (2H, t), 6.90 (2H, d), 7.52 (2H, d), 7.66 (4H, q) ppm.

2.1.2. 4′-(11-Hydroxyundecyloxy)biphenyl-4-carboxylic acid, 9. Compound **8** (5.00 g, 0.0137 mol) was heated under reflux in a mixture of sodium hydroxide (2.0 g, 0.05 mol) in ethanol (100 ml) and water (50 ml) for 18 h. On completion, to the cooled reaction mixture (ice bath) conc. HCL was added (until pH 1) and the reaction mixture was stirred for a further 1 h and then filtered. The retained solid was washed with ethanol (60 ml) and then air dried to give a white powdery solid. Yield 5.14 g (98%). ^{1}H NMR (DMSO): δ 1.24 (18H, m), 1.70 (2H, quint), 3.99 (2H, t), 4.36 (1H, broad s), 7.02 (2H, d), 7.66 (2H, d), 7.73 (2H, d), 7.98 (2H, d), 12.90 (1H, broad s) ppm. IR (KBr) ν_{max} 1202, 1256, 1293, 1604, 1686, 2500–3500 cm^{-1}. MS (*m*/*z*) 384 (M^+), 214, 197.

2.1.3. Racemic octan-2-ol, 2. Compound **1** (2.00 g, 0.016 mol) was dissolved in methanol (10 ml) and the solution cooled to below 5°C using an ice bath. Sodium borohydride (0.3 g, 0.008 mol) was added in small portions over 10 min with effervescence. The reaction mixture was stirred at r.t. under nitrogen for a further 1 h. TLC (dichloromethane/ethyl acetate, 9/1) showed a similar spot to commercial octan-2-ol when developed in iodine. Aqueous 10% HCl was added and the reaction mixture was extracted with dichloromethane (2×50 ml) and dried over $MgSO_4$. The solvent was removed *in vacuo* to yield a clear oil. Yield 1.63 g (80%). ^{1}H NMR ($CDCl_3$): δ 0.81 (3H, t), 1.21 (3H, d), 1.21–1.50 (10H, m), 1.79 (1H, br s), 3.72 (1H, sext) ppm. IR ν_{max} 3350, 2961, 2928, 2858, 1466, 1376, 1115 cm^{-1}. MS (*m*/*z*) 112 (M^+-18). Chiral GC Analysis: Optical purity=0 (resolution limit >0.25%) using a Varian Chirosil Dex.CB, 25×0.25 mm column, isothermal at 65°C, helium carrier 60 cm s^{-1} using a Shimadzu 7010 GC. Figure 4 shows a typical analytical Chiral GC trace.

2.1.4. 4-(1-Methylheptyloxycarbonyl)phenyl 4′-(11-hydroxyundecyloxy)biphenyl-4-carboxylate, 10. Compound **6** (1.0 g, 2.6 mmol), compound **9** (0.65 g, 2.6 mmol), EDAC (0.50 g, 2.6 mol) and DMAP (0.20 g)

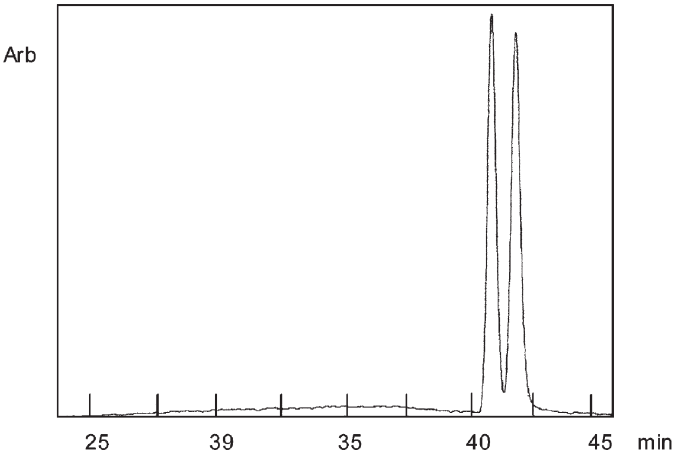

Figure 4. Separation by chiral GC of octan-2-ol **2**, obtained via the reduction of 2-octanone; for details see text.

were stirred together at room temperature in a mixture of dimethylformamide and dichloromethane (30 ml, 3/1) for 4 h. On completion, the solvent was removed *in vacuo* and the product purified by column chromatography over silica (dichloromethane as eluent) and recrystallized from acetonitrile to give a white powder. Yield 1.17 g (73%). ^{1}H NMR ($CDCl_3$): δ 0.88(3H, t), 1.20–1.40 (22H, m), 1.47–1.70 (7H, m), 1.75–1.90 (3H, m), 3.64 (2H, t), 4.02 (2H, t), 5.16 (1H, sext), 7.01 (2H, d), 7.31 (2H, d), 7.60 (2H, d), 7.70 (2H, d), 8.13 (2H, d), 8.23 (2H, d) ppm. IR (KBr) ν_{max} 1290, 1603, 1714, 1732, 2851, 2919, 3200–3600 cm^{-1}. MS (*m/z*) 616 (M^+), 540. Racemate OR: $[\alpha]_D^{27} = -0.00^\circ$; 0.00710 g ml^{-1} in $CHCl_3$; *R*-enantiomer OR: $[\alpha]_D^{20} = -15.94^\circ$; 0.004352 g ml^{-1} in $CHCl_3$; *S*-enantiomer OR: $[\alpha]_D^{23} = +18.43^\circ$; 0.02207 g ml^{-1} in $CHCl_3$.

2.1.5. 4-(1-Methylheptyloxycarbonyl)phenyl 4′-[11-(2-cyclohexylacetoxy)undecyloxy]biphenyl-4-carboxylate,14 *R/S*. Compound **10** (0.25 g, 0.41 mmol), 2-cyclohexylacetic acid (0.06 g, 0.41 mmol), EDAC (0.08 g, 0.41 mmol) and DMAP (0.01 g) were stirred together at room temperature in dichloromethane (25 ml) for 15 h. On completion, the solvent was removed *in vacuo* and the product purified by column chromatography over silica (dichloromethane as eluent) and recrystallized from acetonitrile to give a white powder. Yield 0.23 g (77%). ^{1}H NMR ($CDCl_3$) δ 0.86–1.01(5H, m), 1.20–1.40 (24H, m), 1.47 (2H, quint), 1.53–1.87 (14H, m), 2.17 (2H, d), 4.02 (2H, t), 4.05 (2H, t), 5.16 (1H, sext), 7.00 (2H, d), 7.31 (2H, d), 7.60 (2H, d), 7.70 (2H, d), 8.13 (2H, d), 8.23 (2H, d) ppm. IR (KBr) ν_{max} 1262, 1601, 1720, 1738, 2848, 2922 cm^{-1}. CHN (expected C 76.18, H 8.70; found C 76.11, H 8.92%). OR $[\alpha]_D^{23} = 0.00^\circ$; 0.00258 g ml^{-1} in $CHCl_3$; *R*-enantiomer OR: $[\alpha]_D^{24} = -18.28^\circ$; 0.01634 g ml^{-1} in $CHCl_3$; *S*-enantiomer OR: $[\alpha]_D^{23} = +12.91^\circ$; 0.0101 g ml^{-1} in $CHCl_3$.

2.2. *Evaluation of structural and physical properties*

2.2.1. Phase identification by optical and thermal methods. Phase identifications and determination of phase transition temperatures were carried out by thermal polarized light microscopy using a Zeiss Universal polarizing transmitted light microscope equipped with a Mettler FP82HT microfurnace in conjunction with an FP90 Central Processor. Photomicrographs were obtained using an Olympus BH-2 polarizing light microscope equipped with a JVC digital camera in conjunction with a Mettler FP82HT hot stage and an FP90 temperature controller. Homeotropic sample preparations suitable for phase characterization were prepared simply by using very clean glass microscope slides (washed with water, acetone, water, concentrated nitric acid, water and dry acetone). Homogenous specimens were obtained using untreated glass slides and cover slips, or alternatively by using cells coated with a polyimide aligning agent. Differential scanning calorimetry was used to determine enthalpies of transition and to confirm the phase transition temperatures determined by optical microscopy. Differential scanning thermograms (scan rate 10° min^{-1}) were obtained using a Perkin Elmer DSC 7 PC system operating on Pyris software. The results obtained were standardized to indium (measured onset 156.68°C, ΔH 28.47 J g^{-1}, lit. value 156.60°C, ΔH 28.45 J g^{-1}).

2.2.2. X-ray diffraction studies. The X-ray diffraction experiments were performed on a MAR345 diffractometer equipped with a 2D image plate detector (CuK_α radiation, graphite monochromator, λ=1.54 Å). The samples were heated in the presence of a magnetic field (**B**≈1 T) using a home-built capillary furnace. The diffraction patterns show the intensity as a function of the modulus of the scattering wave vector (q):

$$q = |q| 4\pi \sin\theta/\lambda = 2\pi n/d$$

where θ is the diffraction angle, λ is the wavelength (1.54 Å), n is an integer and d is the lattice distance.

2.2.3. Molecular simulations. Molecular lengths were determined either by using Dreiding molecular models or via computer simulations using an Apple MacIntosh G4 computer and *ChemDraw3D*^{TM} as part of a *ChemDraw Ultra 6.0* program. Space filling models of molecular structures minimized using MM2 computations were obtained using ChemDraw Ultra assuming that the molecular structure was in the gas phase at absolute zero.

2.2.4. Electro-optical measurements. The cells for the electrical field tests were contained within a Mettler FP82HT hot stage oven in conjunction with a Mettler FP90 temperature controller. The hot stage was mounted on a Zeiss Universal microscope fitted with crossed polarizers and an 8/0.2 objective. The applied waveform was supplied by a Hewlett Packard 33120A Arbitrary Waveform Generator into a linear ×20 amplifier (custom-built by QinetiQ). The electrical response from the cell was fed into a nano-current detector (20 kΩ or 100 kΩ impedance) and to a Hewlett Packard 54600B oscilloscope, which was connected to a PC, see figure 5.

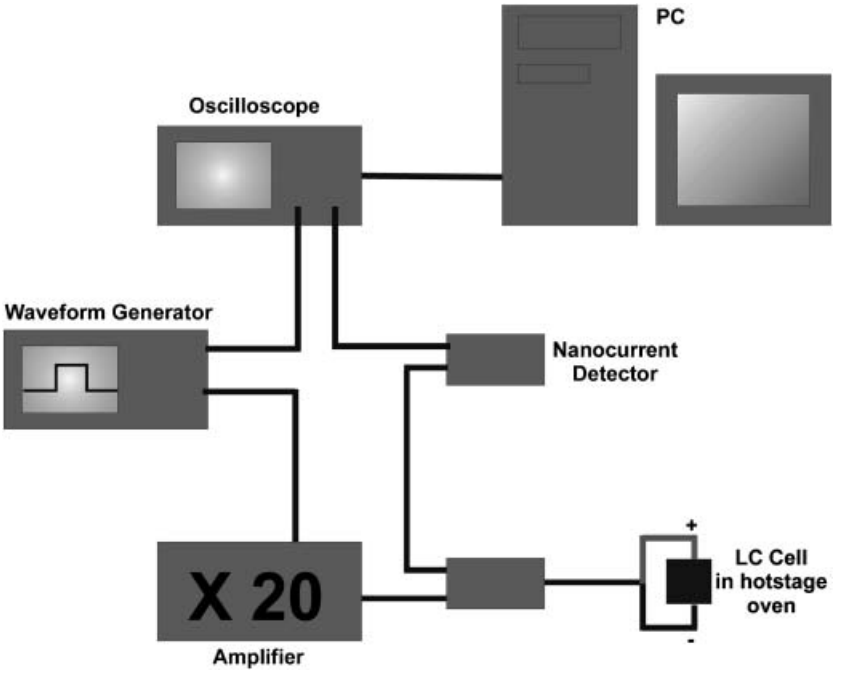

Figure 5. Experimental apparatus for electrical field studies.

The type of cells used in the electrical field studies were constructed from ITO coated glass which had separations of either $1.5 \pm 0.1\,\mu m$ (QinetiQ) or $5 \pm 0.1\,\mu m$ (Linkam), with the internal surfaces coated with a polyimide aligning agent. In the case of the 1.5 μm spaced cells the polyimide coating was buffed in the same direction for each surface (parallel), and for the 5 μm spaced cells the alignment layer was buffed in opposing directions (antiparallel). The cells were filled by capillary action. For the 1.5 μm cells this procedure was aided by carrying out the process in a vacuum oven.

Alignment of the materials was achieved by differing procedures depending on the cell thickness. For the thinner cells, alignment was achieved by slowly cooling the sample from the isotropic liquid into the smectic mesophase, at a rate of $0.1^{\circ}C\,min^{-1}$ and in the absence of any electric field. However, in the cases where the materials exhibited both smectic A and smectic C phases, for thicker cells alignment was achieved by slowly cooling into the smectic A mesophase from the isotropic state, and applying a high electric field in the form of a square wave (typically $16–20\,V\,\mu m^{-1}$) at a frequency of 50 Hz to 1 kHz depending on the material. Once the material was aligned in the cell, the voltage was removed and the cell cooled into the smectic C/C* or C_{alt}/C_A* mesophases. For comparison of results, measurements were determined as a function of the reduced temperature, $T_c - T$, where T_c is the Curie point.

2.2.5. Measurement of spontaneous polarization (using the 5 μm cells). Upon alignment of the liquid crystal, the spontaneous polarization in the tilted phases was determined, on cooling, using a triangular waveform current reversal technique. An a.c. field in a triangular waveform (typically $10\,V\,\mu m^{-1}$ at 30 Hz) was applied to the cell. As the polarization was inverted by the field, a current pulse was observed, and the magnitude of the spontaneous polarization was determined from the area under the current-reversal peak.

2.2.6. Measurement of tilt angle. The determination of tilt angle was achieved by measuring the optical transmission of the switched states using a photodiode (RS303-674; 1 cm^2 active area, high speed >50 ns) in an apparatus custom built by QinetiQ. The equipment was fitted with a green-eye response filter (Coherent-Ealing, 26-7617-000, 1″ diameter, transmittance 400–700 nm, maximum transmittance 539.5 nm). The transmission values were determined using a Thurlby Thandar Instruments 1604 Digital Multimeter.

3. Results

3.1. *Transition temperatures*

The transition temperatures, enthalpies of transition, tilt angles and values of the maximum spontaneous polarization for materials **11** to **17** (*R*/*S, R and S*) are given in table 2. Similarly, in table 3 analogous results

Table 2. The phase classification, phase transition temperatures (°C), enthalpies of transitions (ΔH, kcal g^{-1} relative to an indium standard [9]), switching angles (°), and the maximum values of the spontaneous polarization nC cm^{-2} for materials **11** to **17** (*R/S, R and S*).

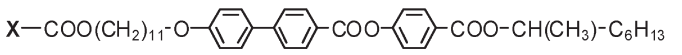

Terminal Group *X*	Compound	
$CH_2=CHCH_2$—	**11** (*S*)	Cr 48.1 [54.97] SmC_A* 77.8 [0.05] SmC* 91.1 [1.05] SmA* 95.6 [3.37] I $\mathbf{P}_s$=103, θ=34.5
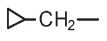	**12** (*S*)	Cr 50.6 [48.83] SmC* 85.3 [0.45] TGBA 87.0 [2.41] I $\mathbf{P}_s$=111, θ=35
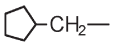	**13** (*R/S*)	Cr 35.7 [57.13] SmC 81.0 [0.79] SmA 87.5 [4.32] I
	13 (*R*)	Cr 37.0 [29.84] SmC* 79.2 [0.8] SmCα* 79.7 [-] TGBA 81.9 [1.81] I $\mathbf{P}_s$=92, θ=36.5
	13 (*S*)	Cr 39.2 [33.08] (SmC_A* 32.0 [-]) SmC* 79.6 [0.94] TGBA 80.7 [2.01] I $\mathbf{P}_s$=99, θ=35.5
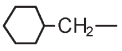	**14** (*R/S*)	Cr 58.4 [73.6] SmC 77.1 [0.4] SmA 83.0 [2.84] I
	14 (*R*)	Cr 56.7 [68.29] SmC* 76.1 [0.86] TGBC 77.0 [-] TGBA 78.1 [1.58] I $\mathbf{P}_s$=93 θ=36
	14 (*S*)	Cr 57.9 [72.18] (SmC_A* 26.2 [-]) SmC* 75.7 [0.53] TGBC 76.4 [1.07] I $\mathbf{P}_s$=98, θ=36
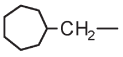	**15** (*R/S*)	Cr 40.0 [54.25] SmC 73.1 [0.74] SmA 79.2 [3.30] I
	15 (*R*)	Cr 40.5 [54.77] (SmC_A* 30.8 [-]) SmC* 70.7 [1.68] I $\mathbf{P}_s$=95, θ=36.5
	15 (*S*)	Cr 45.5 [45.05] (SmC_A* 29.2 [-]) SmC* 70.1 [2.01] I $\mathbf{P}_s$=92, θ=36.5
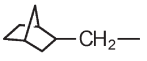	**16** (*R/S*)	Cr 49.0 [67.0] SmCalt 58.2 [-] SmC 74.1 [0.98] SmA 78.4 [3.45] I
	16 (*S*)	Cr 53.9 [53.92] SmX* 59.7 [0.07] SmC_A* 71.5 [3.54] I $\mathbf{P}_s$=101, θ=36.5
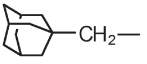	**17** (*R/S*)	Cr 52.1 [60.87] SmC 57.1 [-] SmA 62.3 [1.79] I
	17 (*S*)	Cr 45.7 [31.42] (SmC_A* 40.0 [-]) SmC* 57.4 [1.39] I $\mathbf{P}_s$=89 θ=45

are given for the parent terminally hydroxylated material **10** (*R/S, R and S*). In addition, table 4 lists the transition temperatures of a similar set of known and new materials based on the MHPOBC motif. These materials do not have bulky terminal end groups, and therefore provided reasonable comparisons with the new materials reported. Compound **18**, which is novel, was synthesized for this study to provide a direct comparison of the materials with bulky terminal groups.

The first simple observation that can be made from the tables is that the materials with bulky end units exhibit no SmC_γ (ferri-) and, except for **13**(*R*), no SmC_α phases, suggesting that the interfacial interactions between the layers are important in stabilizing ferri-phases. Unlike the parent analogous materials (see

Table 3. The phase classification, phase transition temperatures (°C), enthalpies of transitions (ΔH, kcal g^{-1}), switching angles (°) and the maximum values of the spontaneous polarization (nC cm^{-2}) for material **10** (*R/S, R and S*).

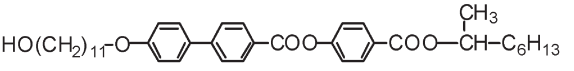

Compound	
10 (*R/S*)	Cr 67.8 [50.52] SmC 96.2 [0.14] SmA 117.3 [7.84] I
10 (*R*)	Cr 83.5 [39.17] SmC* 113.5 [0.75] SmA* 125.0 [5.7] I $\mathbf{P}_s$=103 θ=27
10 (*S*)	Cr 82.8 [59.71] SmC* 115.2 [0.75] SmA*124.7 [7.72]°C I $\mathbf{P}_s$=136 θ=30

Table 4. Transition temperatures (°C) for related known novel materials based on the structure of, and including, MHPOBC.

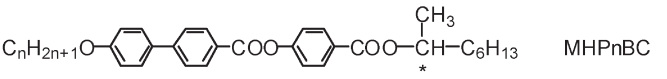

MHPnBC

n	*m*	
8	–	Cr 73.5 (SmI* 62.2) SmC_A* 118.8 Sm$C\gamma$* 119.8 SmC* 121.6 Sm$C\alpha$* 122.6 SmA* 147.7 I [10]
9	—	Cr 59.3 (SmI* 58.0) SmC_A* 105.0 Sm$C\gamma$* 112.1 SmC* 117.9 SmA* 142.2 I [11]
10	—	Cr 67.0 SmC_A* 115.0 SmC* 122.0 SmA* 138.0 I [12]

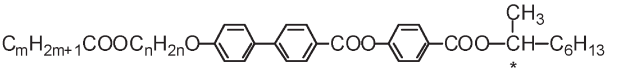

5	4	Cr 72.6 SmC_A* 93.1 SmC* 97.0 SmA* 104.0 I [13]
7	4	Cr 79.7 SmC_A* 90.8 SmC* 93.9 SmA* 100.7 I [13]
5	11	Cr 54.4 SmC_A* 54.6 Sm$C\gamma$* 58.2 SmC* 85.1 SmA* 89.2 I **18**

table 3, and in particular compound **18**), the compounds with bulky end groups exhibit twist grain boundary phases. Remarkably many of the racemic materials exhibit smectic A phases whereas the enantiomers do not exhibit smectic A* modifications.

Similarly, the intermediates with terminal hydroxylated end groups, shown in table 2, were found to exhibit smectic A/A* and smectic C/C* phases, again unlike the final products which have bulky end groups. For the hydroxy-terminated materials the temperature range of the smectic A phase of the racemate **10**(*R*/*S*) is much larger (approximately 23°) than values obtained for the racemic modifications of compounds **11**–**17** (between 4° and 10°). Interestingly the enthalpies of the isotropization points for materials of structure **10** were in most cases more than twice the values determined for materials **11**–**17**. This indicates that the layer structuring for the hydroxy-compounds is stronger than in the materials with bulky end groups. This may be related to the strengthening of the structure caused by intermolecular hydrogen bonding occurring across the layer interfaces.

A more detailed analysis of the trends in transition temperatures is given graphically in figure 6 for the *S*-enantiomers of compounds **11** to **17**. The clearing temperatures are shown to fall linearly with increasing size of the terminal group. The smaller the terminal group the greater the tendency for a material to exhibit orthogonal phases and complex polymorphism. The antiferroelectric phase shows higher thermal stabilities when the terminal group is relatively rigid, i.e. where the terminal group is either small in size, or has a rigid cage structure. The melting points vary most greatly when the terminal group is a flexible ring, but generally the melting points oscillate up and down (+/− 10°C) across the series of compounds about a median of 50°C. Diastereoisomer **16**, which has a structure based on the norbornyl ring system, exhibits anomalous mesophase behaviour when compared with the other materials. The other materials may be considered to have spherical terminal groups because the adamantane unit has a fixed spherical shape and the flexibility of the alicyclic ring systems means that on average they will also be spherical. The norbornyl moiety has a more anisotropic shape which, along with its diastereoisomeric structure may lead to different packing arrangements of the molecules at the interfaces between the layers.

3.2. *Thermal polarized light microscopy*

Initial mesophase classification was achieved by polarized light optical microscopy (POM). Thermal

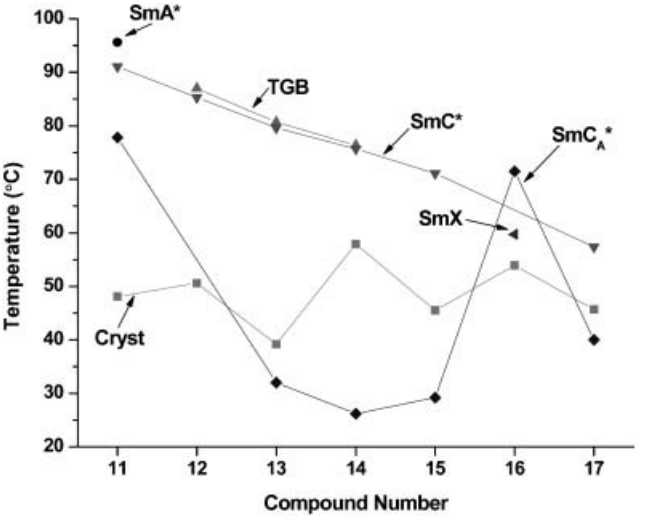

Figure 6. Transition temperature as a function of increasing size of the terminal group (i.e. compound number).

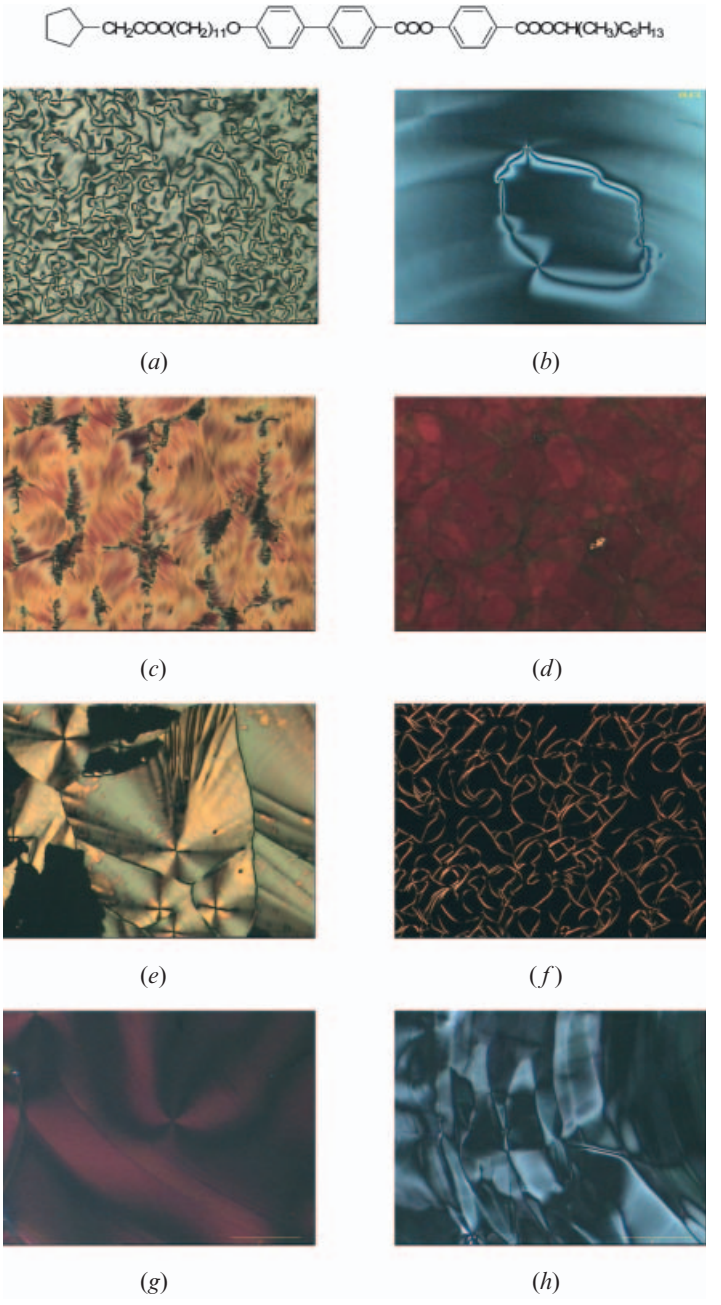

Figure 7. The textures exhibited by materials based on structure **13**: the *schlieren* textures of the smectic C phase of racemate **13**(*R*/*S*), (*a*) between glass plates and (*b*) for a free standing film; the mosaic texture of the TGBA phase (*c*) and Grandjean plane texture (*d*) of enantiomer **13**(*R*); the mosaic texture of the TGB phase (*e*), the filamentary texture of the TGBA phase (*f*), the Grandjean plane textures of the smectic C* phase (*g*) and the antiferroelectric smectic CA* phase (*h*) of enantiomer **13**(*S*), (× 100).

microscopy yielded some interesting and novel textures which are compared in the following section in relation to the differences observed between the racemic modification and the enantiomeric forms of each material.

Figure 7 shows eight different defect textures for the cyclopentyl terminated material **13**. Figures 7 (*a*) and (*b*) show the defect textures of the racemic modification in a supported sample under a glass cover-slip (*a*), and for a free-standing film (*b*). The *schlieren* texture (*a*) is typical of an achiral smectic C phase. Upon rotation of the analyser no colour change was observed, which would indicate that the material is not at all helical, thereby confirming that the material is racemic. The free standing film (*b*) shows that the material exhibits

loops/defect walls. When the *R*-enantiomer was examined a twist grain boundary phase formed first from the isotropic liquid; an example of the texture that this phase exhibits is shown in (*c*) for the material contained within a 5 μm cell. When the enantiomer is obtained in its smectic C* phase an iridescent petal texture is obtained, at approximately 35°C, as shown in (*d*). The colour shows that the pitch of the phase is comparable to the wavelength of visible light, *i.e.* 0.4–0.7 μm. Comparison of (*a*) and (*d*) gives an indication to the relationship between optical purity and helical pitch length. Textures (*e*) to (*h*) are typical examples of defect patterns exhibited for the *S*-enantiomer. Plates (*e*) and (*f*) show the textures of the twist grain boundary phase, where (*e*) is the texture obtained in a 5 μm cell and (*f*) is the typical filamentary texture obtained for a specimen sandwiched between a slide and cover-slip. The filamentary texture confirms that the twist grain boundary phase that is exhibited is a TGBA phase. Figure 7 (*g*) shows the petal texture for a free standing film of the helical smectic C* phase, and (*h*) shows the subsequent *schlieren* texture of the antiferroelectric SmC_A* phase formed on cooling. This phase sequence observed for the *S*-enantiomer differs from that of the *R*-enantiomer in that the *S*-isomer possesses an anticlinic phase in addition to a synclinic modification. The introduction of the anticlinic phase is indicative of the higher optical purity of the *S*-enantiomer.

Figure 8 shows eight textures for the racemic, *R*- and *S*-enantiomeric forms of the cyclohexyl-terminated material **14**. Figures 8 (*a*) and (*b*) show the *schlieren* and focal-conic forms of the smectic C phase of the racemate. The *schlieren* texture is typical of an achiral smectic C phase; it shows no colour change upon rotation of the analyser, indicating that the phase has no helical structure. The focal-conic texture (*b*) was obtained when the material was placed in a 1.5 μm cell. This texture is interesting in that grain boundaries between different tilt domains are relatively long and straight, indicating that the tilt has relatively long range ordering on moving from one layer to the next. Figures 8 (*c*) and (*d*) are textures exhibited by the TGB phase of the *R*-enantiomer. From (*c*), where the enantiomer is contained in a 5 μm cell, it might be concluded that the phase is actually a columnar liquid crystal. However, Galerne *et al.* [14] have explained that this type of texture may be formed by twist grain boundary phases. The filamentary texture shown in (*d*) confirms this classification as a TGBA phase. Figures 8 (*e*) to (*h*) show textures exhibited between a glass slide and cover-slip by the *S*-enantiomer: (*e*) shows a very unusual texture for the TGB phase; (*f*) shows the iridescent texture of the smectic C* phase; (*g*) shows the transition to the antiferroelectric phase; and (*h*) shows the texture of the fully formed antiferroelectric phase, the lack of iridescence indicating that the pitch length of the helical structure in this phase was considerably longer than in the chiral smectic C phase.

The helical twist direction for all of the materials tested followed the Goodby–Chin rules for ferroelectric liquid crystals, the *S*-enantiomers gave left-handed helices (Sol), whereas the *R*-enantiomers gave right-handed helices (Rod).

The norbornyl-terminated material **16** exhibited some unusual defects in its antiferroelectric phase. Multiple brushed defects, e.g. $S=2$, were observed. These defects were either derived from complex singularities, screw dislocations or dispirations [15], or else they were formed by two singularities coming close together. A free-standing film of the *S*-enantiomer is shown in figure 9.

3.3. *Differential scanning calorimetry*

The enthalpies of transition for all of the compounds **11**–**17** are shown together in table 1. Apart from confirming the transition temperatures, differential scanning calorimetry also served to demonstrate the differences between the enantiomers and their racemic modifications. The isotropization points were shown to be sensitive to optical purity, with the racemic modifications clearing at as much as 8°C higher than the enantiomer of greater optical purity. These results are similar to those obtained for many other systems where twist grain boundary (TGB) phases are exhibited by the enantiomers [16]. The extensive lowering of the isotropization points for enantiomers **13**(*R*) and **13**(*S*) in comparison to the racemic modification **13**(*R*/*S*); and enantiomers **14**(*R*) and **14**(*S*) relative to racemate **14**(*R*/*S*), are strong indicators of the fact that the optical purities of the racemic modifications are close to, or are, zero.

Furthermore, for all of the enantiomers a thermal event was found to take place in the isotropic liquid just before the isotropization points. This effect is associated with the transition to structurally frustrated TGB phases *via* the formation of proposed entangled or disentangled flux phases, in analogy with such phases formed by type II superconductors [17]. Interesting similar thermal effects were also observed before the transitions from the liquid state for materials that exhibited either isotropic liquid to smectic C* or isotropic liquid to smectic C_A* phase transitions.

In addition, the phase transition from the smectic A to the smectic C phase in the racemic modifications, and the TGB phase to the chiral smectic C* phase in the enantiomers, appeared to be first order rather than typically second order, see for example figure 10 for the *R*-, *S*- and racemic forms of compound **13**.

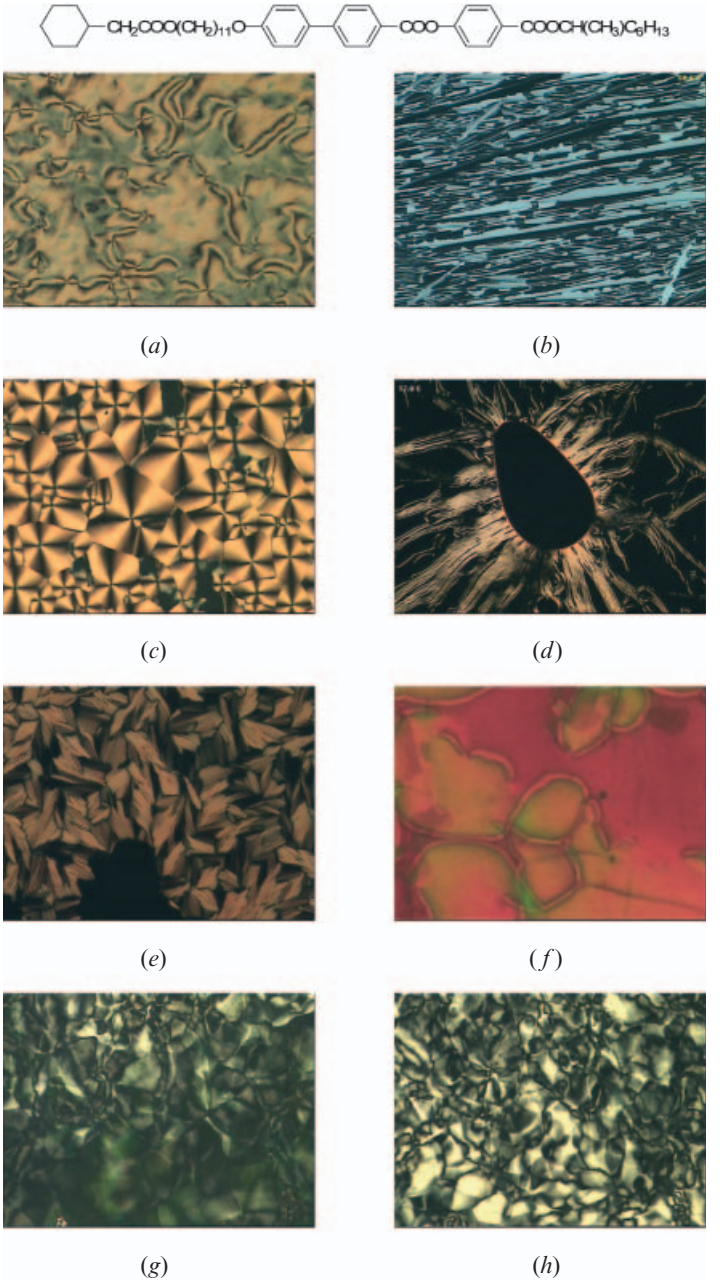

Figure 8. The textures exhibited by materials based on structure **14**: the *schlieren* (*a*) and the focal-conic (*b*) textures of the smectic C phase of racemate **14**(*R*/*S*); the spherulitic (*c*) and filamentary (*d*) textures of the TGBA phase of enantiomer **14**(*R*); the mosaic texture of the TGB phase (*e*), the Grandjean texture of the smectic C* phase (*f*), and the transition (*g*) to the antiferroelectric smectic C_A* phase (*h*) of enantiomer **14**(*S*), ($\times 100$).

3.4. *X-Ray diffraction*

X-ray diffraction studies on aligned and unaligned specimens of the racemic and enantiomeric forms of materials **13**, **14** and **15** were performed as a function of temperature. A representative example for the cyclopentyl compounds, **13**, is shown in figure 11. In each figure the narrow and wide angle scattering and the layer spacing as a function of temperature are shown for comparison.

In all cases the X-ray patterns obtained were for layered phases with disorganized arrangements of their constituent molecules. For example, the results obtained for the racemic modification of compound **13** are shown in the top part of figure 11. In the wide angle region

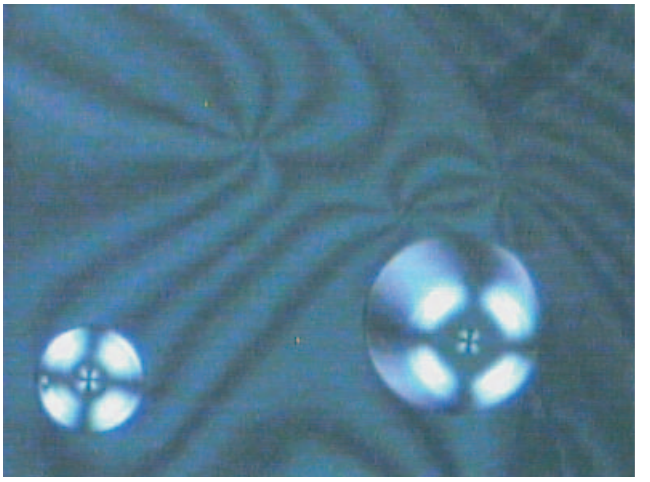

Figure 9. The *schlieren* texture obtained for a free-standing film of the *S*-enantiomer of compound **16** at 45°C (× 100).

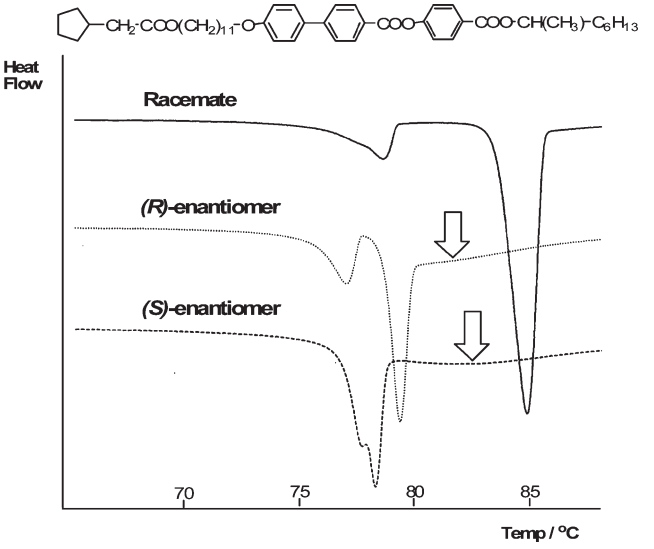

Figure 10. Differential scanning thermograms as a function of temperature, at a cooling scan rate of 10°C min^{-1} for the racemic modification, *R*-enantiomer and *S*-enantiomer of material **13**. The arrows show a thermal event occurring in the isotropic liquid for both enantiomers.

(centre figure) the broad diffuse peaks are related to lateral positional order between the molecules, which can be seen to be uncorrelated and diffuse. In the small angle region (left-hand figure), strong reflections can be seen related to the correlations between the layers of each mesophase. At low temperatures the layer spacings are at a higher q value in the tilted smectic C phase, than they are in the smectic A phase.

The layer spacing as a function of temperature is shown in the right-hand part of the figure. For the racemate, the smectic A layer spacing was found to be approximately 41.25 Å. As the temperature is lowered further the transition to the smectic C phase is marked by a rapid decrease in the layer spacing over a temperature range of approximately 5°C, upon which the layer spacing becomes temperature independent. This behaviour is not typical of a smectic C phase formed from an A phase via a second order phase transition, in this case the layer spacing would be expected to fall and eventually level off with falling temperature.

For the *R*- and *S*-enantiomers, a similar pattern of behaviour was found in the racemic modification, except for the changes which occur near to the clearing points. For the enantiomers, TGB phases are exhibited rather than the smectic A phase found for the racemate. The layer spacings shown in the right-hand figures show that they are commensurate with the TGB phases being of the A type, i.e. TGBA. In the liquid phase near to the clearing points for both enantiomers strong reflections are observed, which would suggest an increase in ordering in the isotropic liquid near to the transition to the TGB phase. Moreover, the TGBA phase does not stay stable for long, with the layer spacing falling rapidly as the temperature is lowered. The layer spacings in the smectic C* phases of both enantiomers remain relatively constant over a wide temperature range. Interestingly, the layer spacing is slightly higher for the *R*-enantiomer than for the *S*-enantiomer. This means that the tilt angle for the *S*-enantiomer is larger than for the *R*-enantiomer.

For materials **14** and **15** similar behaviour is observed, except that compound **15** does not exhibit a TGB phase. Nevertheless, for both of these materials the low angle scattering data show even stronger reflections occurring near to the clearing points, which indicates that there is considerable ordering occurring in the liquid state. Furthermore, the temperature range over which the layer spacing is commensurate with the presence of a TGBA phase for compound **14** is so short that in actual fact the TGB phases are mostly tilted phases, i.e. they are TGBC phases.

4. Electro-optical studies of the chiral materials

4.1. *Tilt angle measurements*

The optical tilt angles were determined as a function of temperature as described in the experimental section. Figure 12 shows the tilt angles as a function of reduced temperature for the *S*-enantiomers of compounds **11** to **17**. The tilt angle for materials **11** to **16** typically rises and then levels off as the temperature falls. The temperature over which the rise occurs is approximately 20°C, which is about 10°C more than the range over which it rises when determined by X-ray diffraction. For the *S*-enantiomer of compound **17**, as the material exhibits a direct transition

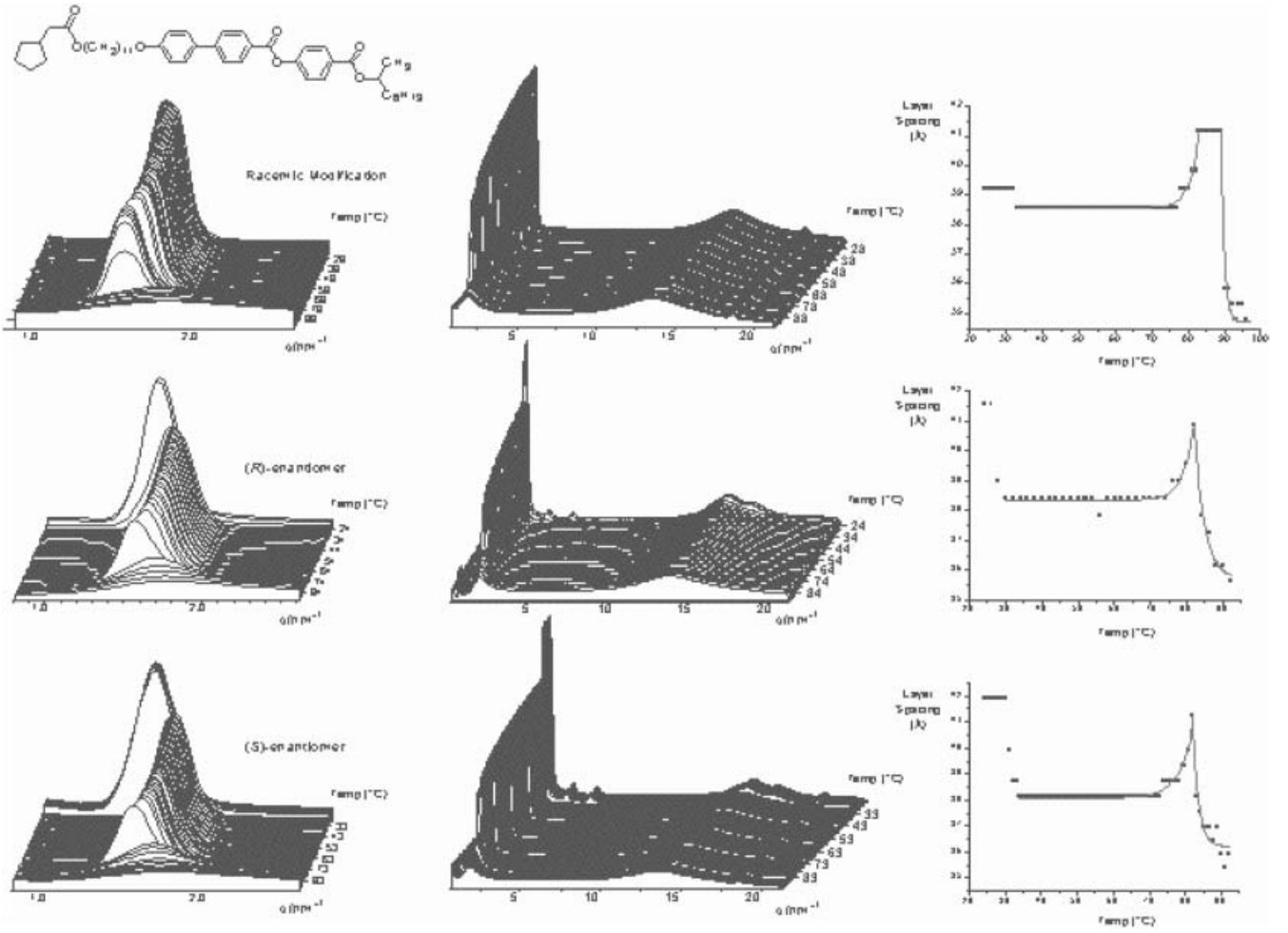

Figure 11. X-ray diffraction results for materials **13**(*R*/*S*), **13**(*R*) and **13**(*S*). The left-hand figures show the small angle scattering region, the centre figures show the small and wide angle scattering as a function of temperature (°C), and the right-hand figures show the layer spacing (Å) as a function of temperature (°C).

from the liquid to the smectic C* phase, the tilt angle is independent of temperature, and has a relatively high value of approximately 45°. The comparative tilt angle for the whole set of materials shows that as the terminal group increases in size, so too does the tilt angle.

4.2. *Spontaneous polarization measurements*

The spontaneous polarization was determined as a function of the reduced temperature as described in the experimental section. Figure 13 groups all of the materials together in graphical form. For all of the materials, including compound **17** which has a temperature-independent tilt angle of 45°, the spontaneous polarization jumps near the Curie point, then rises and almost levels off as each material approaches recrystallization. The results for compound **16**, which exhibits an antiferroelectric phase on cooling from the isotropic liquid, also follow the same pattern in switching between its ferroelectric states.

Interestingly the materials with the higher tilt angles, i.e. **17**, **16**, **15** etc., have the lower spontaneous polarization values. This is probably due to a volume factor because the spontaneous polarization is dependent on the dipoles per unit volume, and as the terminal group size increases in volume so the spontaneous polarization falls. Yet at the same time the tilt angle increases with increasing size of the terminal groups, which means that the spontaneous polarization also should increase with the tilt angle. The curves for all of the materials are compared together in figure 13.

5. Discussion

5.1. *Mesophase structures*

The results of this work show that by incorporating a bulky, apolar, terminal group into chiral materials based on the MHOPBC motif, orthogonal and ferrielectric phases are suppressed. For example,

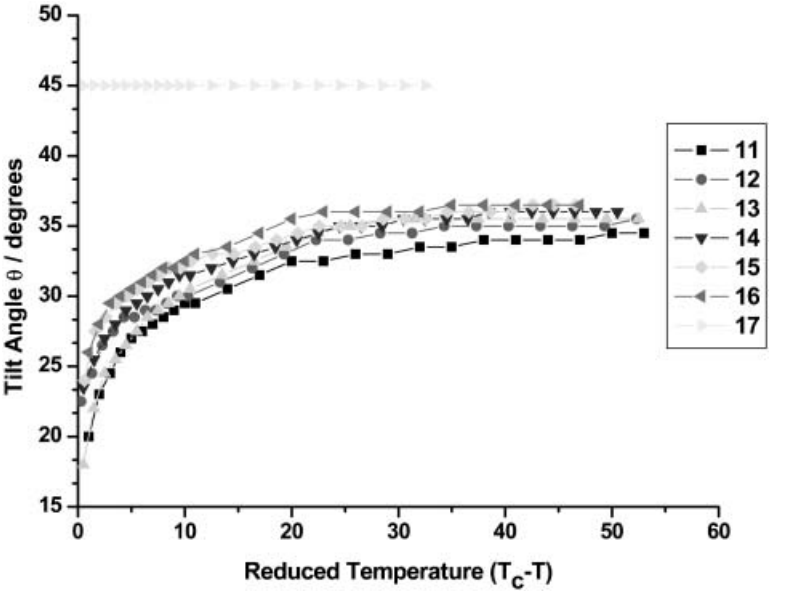

Figure 12. The optical tilt angle determined from electric field studies as a function of reduced temperature for the *S*-enantiomers of materials **11** to **17**.

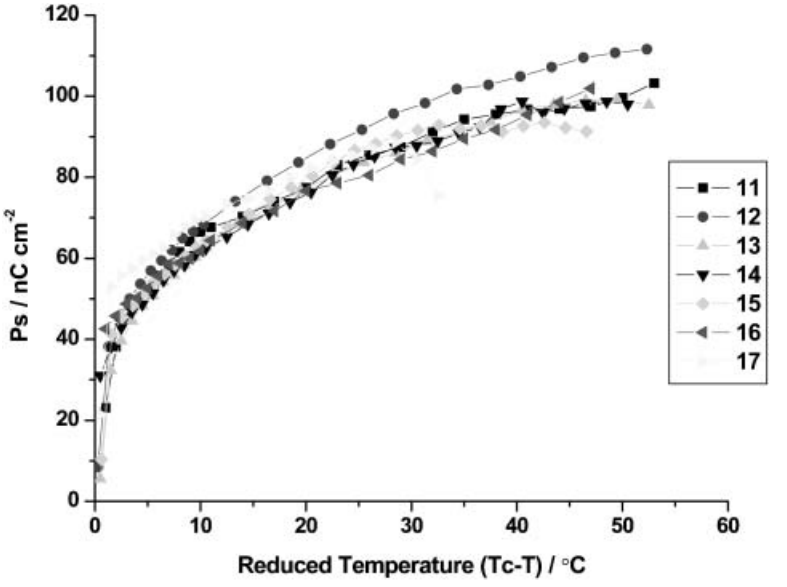

Figure 13. Spontaneous polarization as a function of the reduced temperature for the *S*-enantiomers of compounds **11**–**17**.

the straight chain analogue **18** (see comparable data in table 4) exhibits a typical A*, C*, C_{ferri}* and C_A* phase sequence, whereas a number of the chiral materials possessing bulky terminal groups exhibit TGB phases, suggesting that the layer ordering is much weaker in these materials in comparison with the straight chain analogues. The racemic materials with bulky end groups, on the other hand, exhibit smectic A phases. This suggests that layers are weak enough in the SmA phase to be broken up by an in-plane twist induced when chirality is introduced into the system, i.e. in the formation of TGB phases [18]. Similarly, for many of the bulky end group materials there is no anticlinic phase. It has been suggested that interlayer interactions drive the introduction of the alternating tilt [19]. Weakening these interactions would be expected to drive the system towards being synclinic.

These observations suggest we may be affecting the interlayer packing and related interactions, and if this is the case we might also expect to observe in-plane

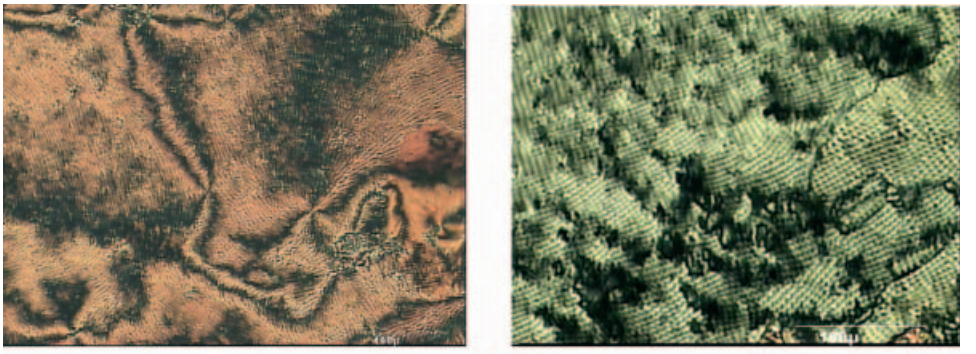

(*a*) (*b*)

Figure 14. The cross-hatched textures of the racemate **14**(*R*/*S*).

ordering in the structures of the smectic phases. It is known that in TGB phases in-plane modulations and superlattices can be manifested as cross-hatched regions in homeotropic textures observed in the microscope, as described by Madhusudana *et al.* [6] and Clark *et al.* [20]. Thus we sought to find such regions in the *schlieren* textures of the materials reported in this work. Although we could not detect such cross-hatching in the chiral materials, figures 14 (*a*) and (*b*) show cross-hatched *schlieren* textures for the smectic C phase for the racemic modification of compound **14**. While such cross-hatching may be due to flow effects in the SmC phase, its presence could also support the view that the materials with bulky end groups may have in-plane ordering of the molecules, resulting in a mesophase with a novel structural form, such as that shown in figure 2 (*d*). Should this be the case, this result indicates that, apart from the $\widetilde{\mathrm{A}}$ and $\widetilde{\mathrm{C}}$ phases, there are a number of other possible structures for smectic phases which have hitherto remained undetected, some of which are shown in figure 15 [21].

6. Conclusions

In this study we have shown that by incorporating a bulky terminal group, the formation of SmC_{γ} and $\mathrm{SmC_A}$ phases are destabilized such that we no longer observe SmC_{γ} phases at all. In the chiral materials, the bulky groups favour the formation of TGB phases over the formation of SmA phases, presumably due to weakened interlayer interactions derived from an increase in the volume of the terminal group. The

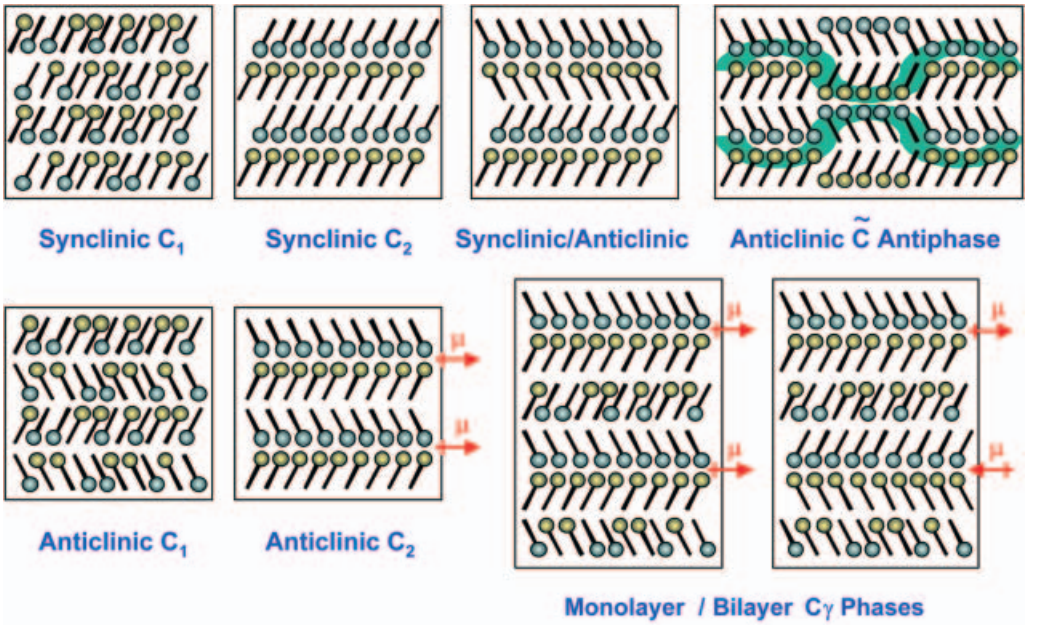

Figure 15. Some possible layer structures of materials with segregating end-groups [21].

increase in the volume of the terminal group favours the formation of tilted phases, i.e. TGBC and ultimately SmC phases. We also suggest that the inclusion of bulky terminal groups into the molecular structures of the liquid crystals can have the effect of inducing in-plane modulations or undulations, which could, if strong enough, lead to novel mesophase formation where the modulations are in-phase or out-of-phase.

Acknowledgement

We thank the Engineering and Physical Sciences Research Council (EPSRC) and Kingston Chemicals Ltd (UK) for financial support. We also thank Dr P. Kouwer for technical support with the X-ray diffraction experiments, Mrs J.A. Haley for technical assistance with differential scanning calorimetry, Mrs B. Worthington for assistance with NMR spectroscopy and determining optical rotations, and Mrs C. Kennedy for elemental analysis.

References

[1] J.W. Goodby. *J. mater. Chem.*, **1**, 307 (1991).
[2] I. Nishiyama, J.W. Goodby. *J. mater. Chem.*, **2**, 1015 (1992); I. Nishiyama. PhD Thesis, University of Hull (1992); S.-E. Lee. PhD Thesis, University of Hull (1998); S.J. Cowling. PhD Thesis, University of Hull (1999); G. Cosquer. PhD Thesis, University of Hull (2000); J.W. Goodby. In *Dynamics and Defects in Liquid Crystals: A Festschrift in Honour of Alfred Saupe*, P.E. Cladis and P. Palffy-Muhoray (Eds), pp 273–291. Gordon and Breach, Amsterdam (1998).
[3] J.W. Goodby, G.W. Gray, D.G. McDonnell. *Mol. Cryst. liq. Cryst. Lett.*, **34**, 183 (1997); J.W. Goodby, and G.W. Gray. *Mol. Cryst. liq. Cryst. Lett*., **41**, 145 (1978); J.W. Goodby and G.W. Gray. *J. Phys. (Paris), C3*, **40**, 27 (1979); J.W. Goodby, G.W. Gray. *Mol. Cryst. liq. Cryst.*, **37**, 157 (1976).
[4] K. Terashima, M. Ichihashi, K. Kikuchi, T. Inukai, *Presented at the 11th International Liquid Crystal Conference*, San Francisco (1986), A.D.L. Chandani, T. Hagiwara, Y. Suzuki, Y. Ouchi, H. Takezoe, A. Fukuda. *Jpn. J. appl. Phys.*, **27**, 729 (1988); K. Miyachi, A. Fukuda. In *Handbook of Liquid Crystals Vol 2B:* D. Demus, J.W. Goodby, G.W. Gray, H.-W. Spiess and V. Vill (Eds), pp 665–691. Wiley-VCH, Weinheim, (1998).
[5] F. Hardouin, G. Sigaud, N.H. Tinh, M.F. Achard. *J. Phys (Paris) Lett.*, **42**, 63 (1981); F. Hardouin, N.H. Tinh, M.F. Achard, A.-M. Levelut. *J. Phys (Paris) Lett.*, **43**, 327 (1982).
[6] P.A. Pramod, R. Pratibha, N.V. Madhusudana. *Curr. Sci.*, **73**, 761 (1997); C.V. Yelamaggad, S.A. Nagamani, U.S. Hiremath, D.S.S. Rao, S.K. Prasad. *Liq. Cryst.*, **28**, 1581 (2001); P.A. Pramod, Y. Hatwalne, N.V. Madhusudana. *Liq. Cryst.*, **28**, 525 (2001).
[7] D. Brown. *Int. J. med. Microbiol.*, **291**, 433 (2002).
[8] E. Chin, J.W. Goodby. *Mol. Cryst. liq. Cryst.*, **141**, 311 (1986).
[9] R.C. Priest (Ed.). *CRC Handbook of Physics and Chemistry*, 68th Edn, CRC Press, Boca Raton (1988).
[10] A.D.L. Chandani, E. Goreka, Y. Ouchi, H. Takezoe, A. Fukuda, K. Terashima, K. Furukawa, A. Kishi. *Jpn. J. appl. Phys.*, **28**, L1265 (1989).
[11] W.K. Robinson, H.F. Gleeson, M. Hird, A.J. Seed, P. Styring. *Ferroelectrics*, **178**, 249 (1996).
[12] T. Kusumoto, K. Ogino, T. Hiyama, T. Isozaki, Y. Suzuki. *Chem. Lett.*, 865 (1996).
[13] W. Drzewinski, R. Dabrowski, K. Czuprynski. *Polish J. Chem.*, **76**, 273 (2002).
[14] A.C. Ribeiro, A. Dreyer, L. Oswald, J.F. Nicoud, A. Soldera, D. Guillon, Y. Galerne. *J. Phys (Paris) II*, **4**, 407 (1994).
[15] Y. Takanishi, H. Takezoe, A. Fukuda, H. Komura, J. Watanabe. *J. mater. Chem.*, **2**, 71 (1992).
[16] J.W. Goodby, I. Nishiyama, A.J. Slaney, C.J. Booth, K.J. Toyne. *Liq. Cryst.*, **14**, 37 (1993).
[17] P.G. de Gennes. *Solid State Commun.*, **10**, 753 (1972).
[18] J.W. Goodby, M.A. Waugh, S.M. Stein, E. Chin, R. Pindak, J.S. Patel, *Nature*, **337**, 449 (1989); J.W. Goodby, M.A. Waugh, S.M. Stein, E. Chin, R. Pindak, J.S. Patel. *J. Am. chem. Soc.*, **111**, 8119 (1989).
[19] J.W. Goodby. In *Structure and Bonding - Liquid Crystals II*, D.M.P. Mingos (Ed.), p. 83, Springer Verlag, Berlin, Heidelberg (1999).
[20] N.A. Clark. Personal communication.
[21] I. Nishiyama, J.W. Goodby. *J. mater. Chem.*, **2**, 1015 (1992).